



Robust scanning of AEM data for IP effects

Andrea Viezzoli^a, Francesco Dauti^b and Chris Wijns^c

^aAarhus Geophysics Aps, Risskov, Denmark; ^bDepartment of Geosciences, Università di Pisa, Pisa, Italy; ^cFirst Quantum Minerals Ltd, Perth, Australia

ABSTRACT

The industry has widely accepted that AEM data are more frequently affected by induced polarisation (IP) effects than previously acknowledged. However, we still lack a clear understanding of how much, where, and when IP is present. Full modelling of airborne IP (AIP) is time and computationally intensive. As an alternative, we derive a novel tool, the “AIP scanner”, based on a combination of extensive data – space and limited model – space analysis. The basic assumption is that failing to model IP, when present, increases AEM inversion misfits. Several data space metrics, on negatives and on decay rates, are correlated to misfit from inversion ignoring IP over a small portion of the dataset. The correlation is used to predict the presence of AIP over the entire dataset. The last step is a recursive comparison between the map of predicted AIP and the results of full AIP modelling over a few selected lines. The resulting “AIP scanner” map indicates areas of definite AIP effects, areas possibly affected, and areas probably unaffected by AIP. Such maps are extremely useful tools for the exploration industry wishing to leverage AEM data information content. A case study from South Australia illustrates the scanner results relative to mapped geology and demonstrates the relationships between chargeability and the often unpredictable consequences for the resistivity inversions.

ARTICLE HISTORY

Received 30 April 2020
Accepted 21 November 2020

KEYWORDS

Airborne electromagnetics; induced polarisation; processing; conductivity; exploration methodologies; modelling

Introduction

It has long been recognised that negative voltages recorded by AEM systems in concentric loop configurations cannot be reconciled with non-dispersive resistivity models normally used to model the AEM data (e.g. Smith and West 1988). Such negative voltages require models accounting for the dispersive nature of resistivity, i.e. for induced polarisation (IP) effects. More recent research (Viezzoli and Manca 2020) has shown that, without ever causing negatives, IP effects can distort the transients to such a degree that they will produce artefacts in the resistivities (conductivities) recovered, unless modelled taking dispersive resistivity into account. The industry is therefore starting to accept that airborne IP (AIP) effects must be accounted for, as they are more widespread than previously acknowledged. The relevance to the exploration of the chargeability models derived from AIP, and their relationship to standard ground IP survey results, is still uncertain.

Full AIP modelling is more time consuming than standard modelling. The reason is twofold: data processing is less suited to automation, requiring more visual inspections and manual editing; inversions are more ill posed, demanding slower, safer convergence strategies within each inversion, and more thorough numerical experiments to reduce non-uniqueness and produce a realistic output (cf. Viezzoli, Kaminski, and Fiandaca 2017, for more details on inversion strategies). Consequently, it is desirable to carry out AIP modelling

only where needed. As a short cut, some contractors produce maps of “apparent chargeability” based on a combination of early-time resistivity inversions and late time decays (Kwan et al. 2015) or using negative voltages (Chen, Hodges, and Smiarowsky 2015) to describe the presence of AIP effects. We maintain that both of these approaches are an oversimplification and can lead to erroneous conclusions regarding the presence or absence, amount, and source type of actual IP effects in the data. A novel and more robust method for assessing the presence of IP effects in AEM data, which we term the “AIP scanner”, is based on the joint analysis of the entire data space together with a selected portion of the model space.

Methods and results

Viezzoli and Manca (2020) show, with synthetic examples, how complex the correlation between data and model space is in the presence of chargeability. They also present metrics (e.g. negatives and rates of decay) that, used together, can capture the main signatures of IP in AEM data. On the other hand, researchers including Kaminski and Viezzoli (2017), Oldenburg and Kang (2015), and Macnae (2016) show, on field data, how complex the recovered chargeability models can be. They also prove that failing to model IP, when present, usually increases data misfit. Summarising, IP effects in AEM data can (a) produce negatives, (b) increase the

decay rate of transients, and (c) if not modelled, result in large data misfits associated with inverted resistivity models. We merge these findings originating from data and model space into the “AIP scanner”. The main steps are:

- (1) Resample the dataset to approximately 30 m spacing along lines in order to speed up the procedure, without materially affecting the lateral resolution of the AEM system.
- (2) Inspect the voltage data, assess the noise level on the absolute values of voltages, and delete readings below noise.
- (3) Calculate the synthetic responses of the specific AEM system used in the survey to a suite of layered earth scenarios without any chargeability. Fit different portions (e.g. early, mid, late times) of each of these synthetic responses with an exponential decay. Note the upper limit of the range of these decays. They represent the fastest decays and smallest time constants that can be expected without IP effects (IP can increase the rate of decay substantially).
- (4) Run “IP metrics” over the prepared data from point 2. They include metrics both on negative readings and on rates of decay of the transients (cfr Viezzoli and Manca 2020).
- (5) Choose portions of the dataset representing different EM behaviour and invert with layered earth and without IP modelling (i.e. deleting negatives but keeping fast decays). Inspect the resulting misfit.
- (6) Run an optimisation routine (details below) that uses the IP metrics at point 4 to predict the misfits of point 5.
- (7) Use the output of point 6 (i.e. the coefficients associated with the metrics that best predict the misfit in non-IP mode) applied over the entire dataset, obtaining a map: the “AIP scanner”.
- (8) Compare the “AIP scanner” performance against chargeability recovered from selected lines fully modelled for AIP.

Note that step 2 above only deletes gates with values below noise. It does not eliminate those parts of the transient descending more rapidly than they would in the absence of IP, which do enter the following steps.

The forward modelling at point 3 above is carried out over a range of two-layer scenarios that can yield fast decays without calling on IP, i.e., shallow conductive layers over the resistive basement. Systematically varying both the thickness of the first layer and the resistivities of the two layers, we obtain a variety of changes of the slope of the transients over their entire duration. Importantly, we accurately model the AEM system transfer function (waveform, filters, Rx gate times, etc.), and reuse this during inversion at point 5. The rates of decay (often represented using time constant τ) at point 3 and

4 are calculated based on the classic notation by McNeill (1980) over 4–5 gate intervals (of 5–6 gates each), from early to late times. 3D effects can also generate exceedingly fast decays that could be mistaken, locally, for IP effects. In order to avoid potential mischaracterisation of non-polarisable 2D/3D effects, the spatial variation of the different time constants (early, mid, and late times) is inspected for anomalies with short waveforms, either along or across flight lines. If and where present, these are flagged as possible 2D/3D effects (without polarisation) and eliminated with an automated routine based on variograms. They do not affect the remaining steps of the procedure, and no AIP assessment takes place over these areas. We did not assess the potential effect in the routine of polarisable 3D bodies.

The selection of a representative subset to be modelled without IP (point 5) is based on the statistics of the metrics over each line. Note that the selection depends only on signal and is not biased by or guided by geology. The goal is to have a well-balanced sample of EM decays, containing both anomalous and non-anomalous metrics. Further precautions ensure that high misfits are mainly due to IP effects. These include both proper modelling of the known characteristics of the AEM system transfer function during inversions (waveform, filters, attitude) and running several inversions with different starting models and regularisation settings (i.e. constraints), to select those giving the lowest misfit.

The optimisation routine at point 6 uses a subset of the misfits of point 5, equally distributed within their entire range, as observed data. The prediction comes from the linear combination (using the Normal Gaussian matrix formalism) of a number of metrics. These metrics aim for the lowest error in prediction, the simplest answer, the highest level of correlation with misfit, and the lowest level of cross-correlation between each other. They always belong to both groups (at least one based on negatives and one based on decay rates), properly pre-normalised.

The linear problem that we want to solve can be described in the following equation:

$$\begin{aligned} W_{11}M_{11} + W_{12}M_{12} + \dots + W_{1m}M_{1m} &= \text{Misfit 1} \\ W_{21}M_{21} + W_{22}M_{22} + \dots + W_{2m}M_{2m} &= \text{Misfit 2} \\ W_{31}M_{31} + W_{32}M_{32} + \dots + W_{3m}M_{3m} &= \text{Misfit 3} \end{aligned} \quad (1)$$

We solve the problem by calculating the parameters W_m that weigh the corresponding selected metrics M_m to better predict the actual measured misfit.

The set of equations (2–4) describe the optimisation routine in step 6 that predicts misfit based on the linear model described above. \mathbf{d} is an N -dimensional data vector ($\log_{10}(\text{misfit})$), \mathbf{m} is an M -dimensional model parameter vector (the multiplicative coefficients for which we solve), and \mathbf{G} constitutes the $M \times N$ forward operator (Kernel function). This matrix contains the scalar values

of the metrics previously selected as necessary to solve the optimisation with respect to the misfit.

Three preparatory steps are necessary prior to performing this optimisation. First, the elements of \mathbf{d} and \mathbf{G} undergo a subsampling procedure in order to contain mainly fast decay rates and as uniform a distribution of misfit values as possible. Second, as mentioned above, procedures in place to avoid mistaking IP with plausible 3D anomalies on the rates of decay lead to data points being nulled and flagged as free of AIP. Third, given their vastly different magnitudes (e.g. voltages versus decay rates), the different metrics are normalised prior to being inserted in the \mathbf{G} matrix in the following equations.

Equation (2) describes the forward operator:

$$d_{\text{pre}} = \mathbf{G}m \quad (2)$$

where d_{pre} : predicted data ($m \times 1$), \mathbf{G} : inversion operator ($m \times n$) (*Metrics Matrix*), m : unknown coefficients ($n \times 1$).

$$\mathbf{G} = \begin{bmatrix} M_{11} & \cdots & M_{1m} \\ M_{21} & \cdots & M_{2m} \\ M_{31} & \cdots & M_{3m} \\ \vdots & \cdots & \vdots \\ \vdots & \cdots & \vdots \\ M_{n1} & \cdots & M_{nm} \end{bmatrix} \quad d_{\text{obs}} = \begin{bmatrix} \text{misfit}_1 \\ \text{misfit}_2 \\ \text{misfit}_3 \\ \vdots \\ \text{misfit}_n \end{bmatrix}$$

$$m = \begin{bmatrix} m_1 \\ m_2 \\ m_3 \\ \vdots \\ m_n \end{bmatrix}$$

We minimise the relation below using the method of least squares:

$$\min \left[\sum_{i=1}^m (d_{\text{obs}} - (d_{\text{pre}})_i)^2 \right] \quad (3)$$

Obtaining

$$m = (\mathbf{G}^T \mathbf{G})^{-1} \mathbf{G}^T d \quad (4)$$

We perform this optimisation several times, using different combinations of metrics M_{ij} , guided from the linear regressions previously carried out. In each realisation, we calculate the metrics sensitivities (i.e. the Jacobian). This allows us to select the optimisation that requires the least number of metrics, with the highest sensitivities, while keeping the mean squared error in prediction low. We also inspect the spatial and frequency distribution of the prediction errors for each point, seeking the most stationary. The coefficients \mathbf{m} and their associated metrics are applied over the whole dataset, resulting in the “AIP scanner”.

The final comparison at point 8 is between the “AIP scanner” performance in predicting the presence of IP, and full inversion with AIP (as per Viezzoli, Kaminski,

and Fiandaca 2017) over a few lines. This comparison with the model space is important because the AIP scanner does not directly rely on inverted chargeabilities. However, if the underlying assumptions are correct, the scanner results should agree spatially with the inverted chargeability. If they do not, we return to the crucial noise analysis and decay selection of point 2 in the workflow above, restart from there and produce a new version of the “AIP scanner”, until a better correlation is achieved. By experience, the procedure is rather robust and needs no more than two such iterations.

The AIP scanner is unlikely to be affected by superparamagnetic effects (SPM), which are often mentioned in conjunction with AIP effects, though they are due to different physical sources. The typical SPM manifestation of slow decays lasting into late times, suggestive of apparent deep conductors (e.g. Buselli 1982; Sattel and Mutton 2015), will not trigger an AIP scanner anomaly in the procedure described above.

The AIP scanner map defines areas with no measurable AIP effects, areas with definite AIP effects, and areas with possible AIP effects. Although the AIP scanner uses information in both data and model space, its output sits in the data space. That is, it yields neither information about the “quantity” or magnitude of chargeability in the ground nor about the depth or characteristics of the source. This information can only be obtained through modelling the IP effects in the AEM data with an inversion (e.g. using a Cole–Cole model). Recalling that areas with AIP effects yield erroneous resistivity models unless IP is modelled (e.g. both false positive and false negative anomalies, wrong depth to basement), this scanner will indicate where a conventional inversion may wrongly represent conductivity structure, producing either false resistors or conductors.

A case study from South Australia, using data from a recent XciteTM helicopter TDEM survey (Combrinck and Wright 2016), illustrates the extent of AIP distribution and the manner in which including AIP modelling can have a material impact on geological interpretation. The Xcite system deploys a 25 Hz base frequency transmitter injecting a trapezoidal current waveform in the four turns of a loop of approximately 300 m². The receiver, located in the middle of the loop, provides streamed voltage data, later typically binned into 45 gates. The project area sits in the Adelaide Rift Complex, a 1000-km long belt of sedimentary rocks, with some minor volcanics, deposited between 870 and 500 Ma. The local geology, shown in Figure 1, is largely siltstones, sandstones, and dolomite, where carbonaceous siltstones and shales are the most likely candidates for stratigraphic conductors.

Figure 2 shows an extract of the Xcite data along one line, with clear AIP effects as negative voltages indicated in red.

The data were subject to the workflow described above. The noise model applied to eliminate data

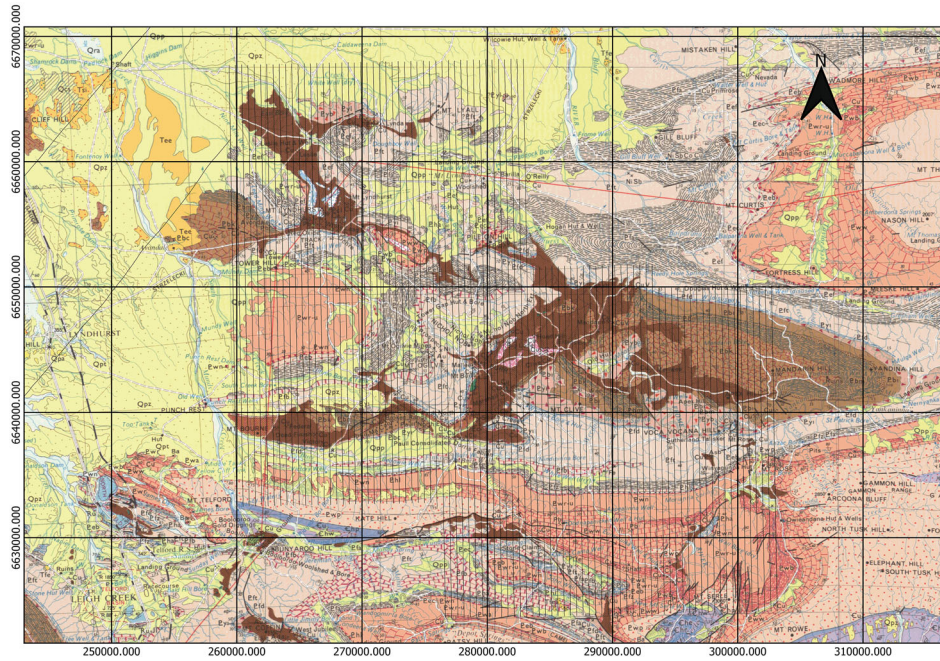


Figure 1. EM survey lines over government geological map. For comparison with AEM images below, dark brown carbonaceous siltstones are the most conductive stratigraphic units, along with light yellow recent cover in the north and west. Medium brown units are dolomite, orange is siltstone and grey/green shales, and pale pink is younger dolomitic siltstone and dolomite.

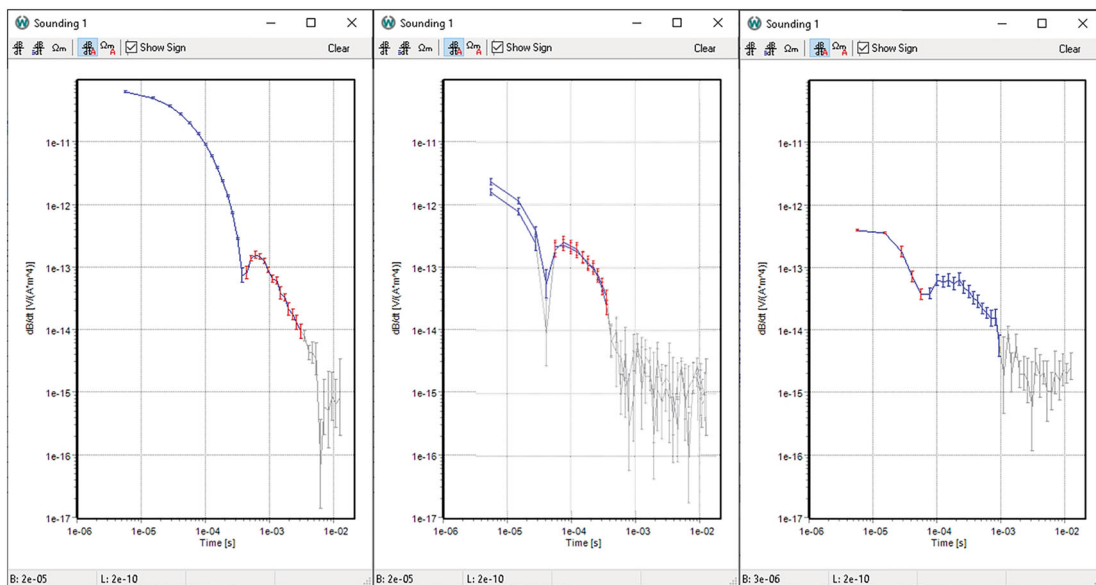


Figure 2. Example of transients affected by IP (red bars represent negative voltages), with late time noise culled and left in light grey. Note how some transients start negative (right plot).

follows the increasing gate widths of the transients. It has a value of 3×10^{-3} pV/Am⁴ at 1 ms, decreasing with longer (i.e. later) time gates according to $\sim t^{-1/2}$. We first calculate metrics on negatives. Figure 3 displays, for example, the sum of $\log_{10}(\text{abs}(\text{negatives}))$. The coherent spatial distribution of the maxima suggests geologic control. The most intense negatives fall within a unit of grey, calcareous shale, and are not particularly aligned with individual stratigraphic units. Unintuitively, while one might assume these represent the strongest IP signals in the dataset, they do not necessarily produce the most material changes between

resistivity sections inverted with and without AIP. As Viezzoli and Manca (2020) show, the strength of a negative response depends on several factors other than the magnitude of chargeability, such as host resistivity or presence of resistive bedrock below the chargeable material. Note also the lack of negative transients over the conductive shales and recent cover, which both present high amplitude signals that IP effects do not overpower.

Table 1 contains calculated EM transient time constants over five groups of representative time intervals (A–E) across the survey area, as described in step 4 of

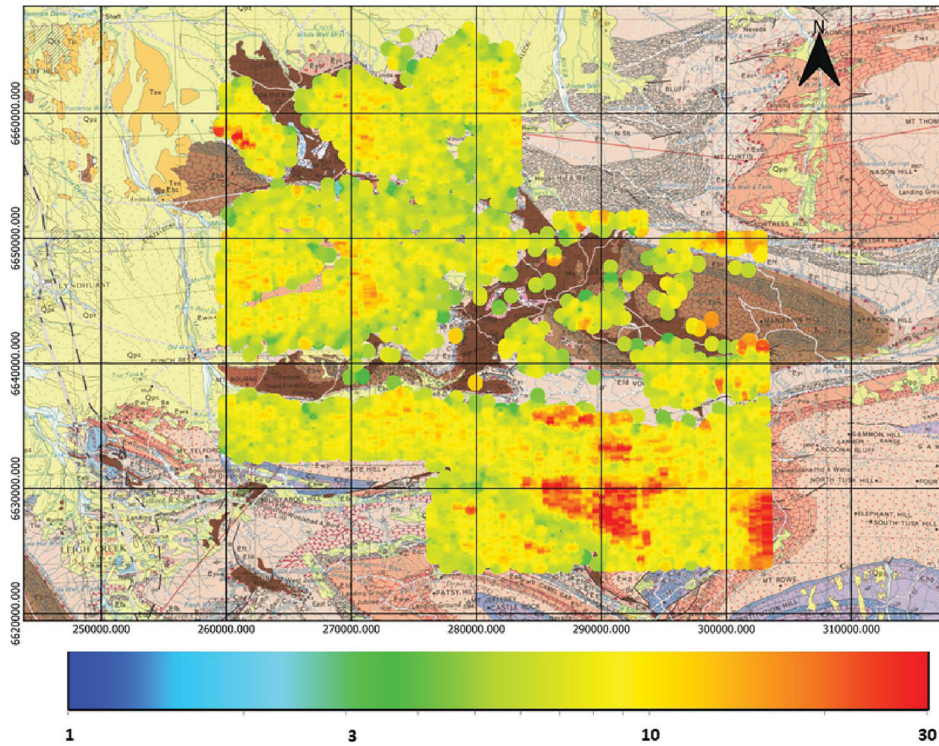


Figure 3. Distribution of sum of $\log_{10}(\text{abs}(\Sigma(\text{negatives})))$, in pV/Am^4 (above noise, see text for details). Blank areas contain no negative values in the transients. These areas are largely over the very conductive shales (brown) and recent cover (pale yellow).

Table 1. Gate intervals (starting from first gate useable for modelling) and corresponding decay rate categories.

Time interval	A	B	C	D	E
Time gates	1–7	8–15	16–21	22–28	29–35
Minimum expected time constant τ (unitless)	0.68	0.41	0.35	0.31	0.22

the workflow. A map of the time constant τ for time interval C is shown in Figure 4. Referring to Table 1, a time constant less than 0.35 on this map cannot be explained without the presence of IP effects. While there is a correspondence with the map of sum of negatives (Figure 3), there are also areas of small τ not associated with negative decays. We elaborate on this point later in the manuscript when describing the sensitivity of this metric.

Given the goal of matching AIP scanner metrics with fully modelled AIP effects, the scanner metrics guide a choice of representative lines, meant to represent areas affected by AIP, to be processed and inverted without AIP modelling. This involves eliminating noisy gates and negatives while keeping the fast decays that also represent the effect of IP. We compare the output misfits of inversion without AIP to the individual metrics previously calculated via a series of scatter plots. Linear regressions are calculated on a subset of all misfits (the \log_{10} of the misfits) and corresponding time constants. As mentioned above in the description of the optimisation routine, the subset is chosen in order to contain mainly fast decay rates and as uniform a distribution

of misfit values as possible. We use time constants up to double the lowest τ value from the non-IP synthetics. Using only the smallest values of τ would result in too small a data sample. This subsampling of the misfit/decay rates plane is required in order to avoid a regression that otherwise would be biased towards the vast majority of non-anomalous decay rates and misfits. This process leads to a selection of time constant intervals that best correlate with the misfits, to be used later in the AIP scanner optimisation routine. Figure 5 shows one of these scatter plots with the corresponding linear regression. A high misfit and low τ will be associated with areas of potential IP.

Following the regression analyses, we optimise for the best combination of coefficients to associate with individual metrics for predicting the misfit obtained without IP, as per step 6 of the procedure explained above. In this case, the best prediction is given by the combination of sum of negatives and decay rates from interval B and C. The sensitivity maps of the AIP scanner to individual metrics (Figures 6–9) are spatially distinct and illustrate how the metrics complement each other in the prediction over the whole area.

Figure 9 shows the final “AIP scanner” map, overlain by high misfit > 1 from inversion without IP, plotted along the lines involved in the prediction. There is a good spatial correlation between the IP scanner and the high misfits. The scanner predicts that approximately 50% of the dataset is affected, to some degree, by AIP. Comparison with Figure 1 also shows the geological control over the AIP scanner, whereby the areas

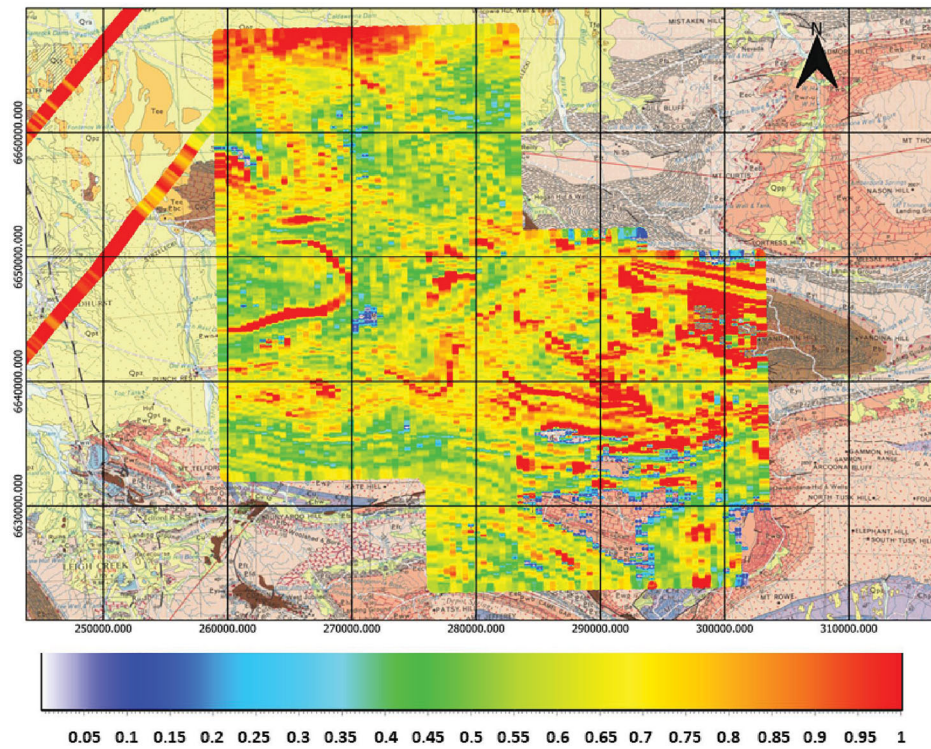


Figure 4. Distribution of time constant τ over interval C (cf Table 1). Blank areas occur where negative decays prevent the calculation of τ .

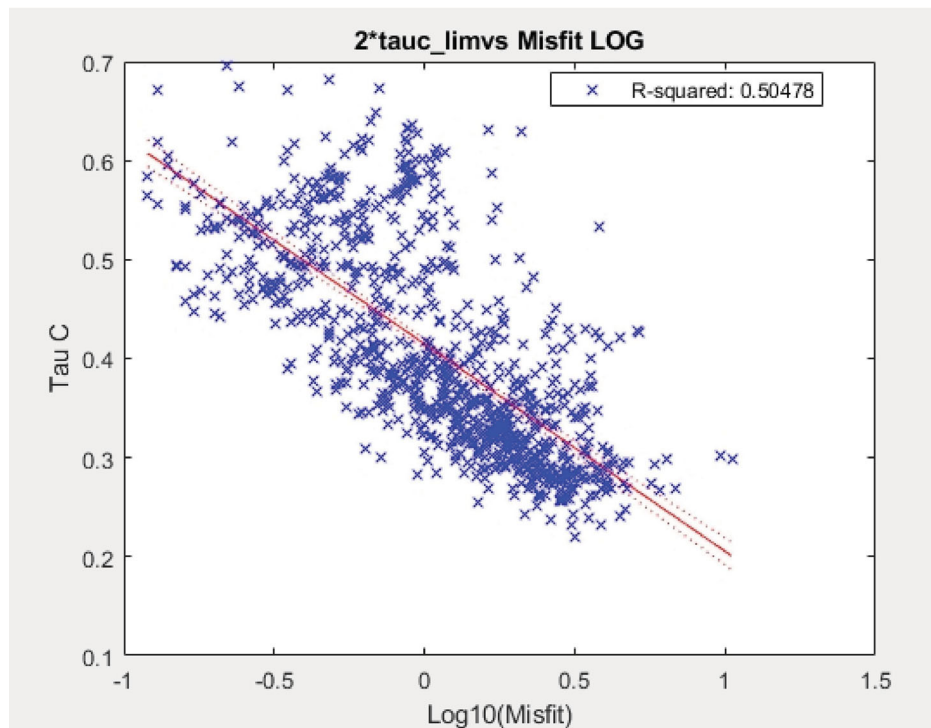


Figure 5. Scatter plot and corresponding linear regression showing correlation between time constant for interval C (refer to Table 1 for detail) and misfit obtained without AIP modelling.

of lower and higher probability of AIP are associated with specific geological units and domains. While the effect of IP on the resulting conductivity inversions may not always be large or even material to interpretation, Figure 9 underlines the widespread occurrence of AIP

effects that one may expect in any AEM dataset in the region.

The last step in the workflow is to carry out AIP modelling over a few selected lines, the same used earlier to invert without AIP. After processing to retain IP

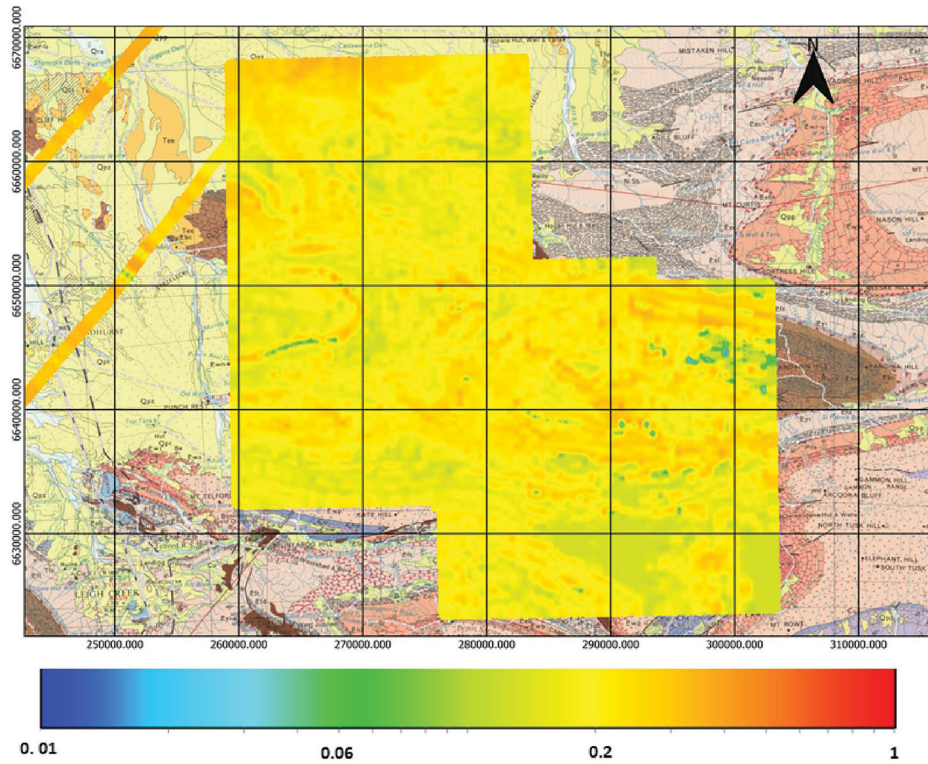


Figure 6. Sensitivity of IP scanner to the metric of decay rate interval B.

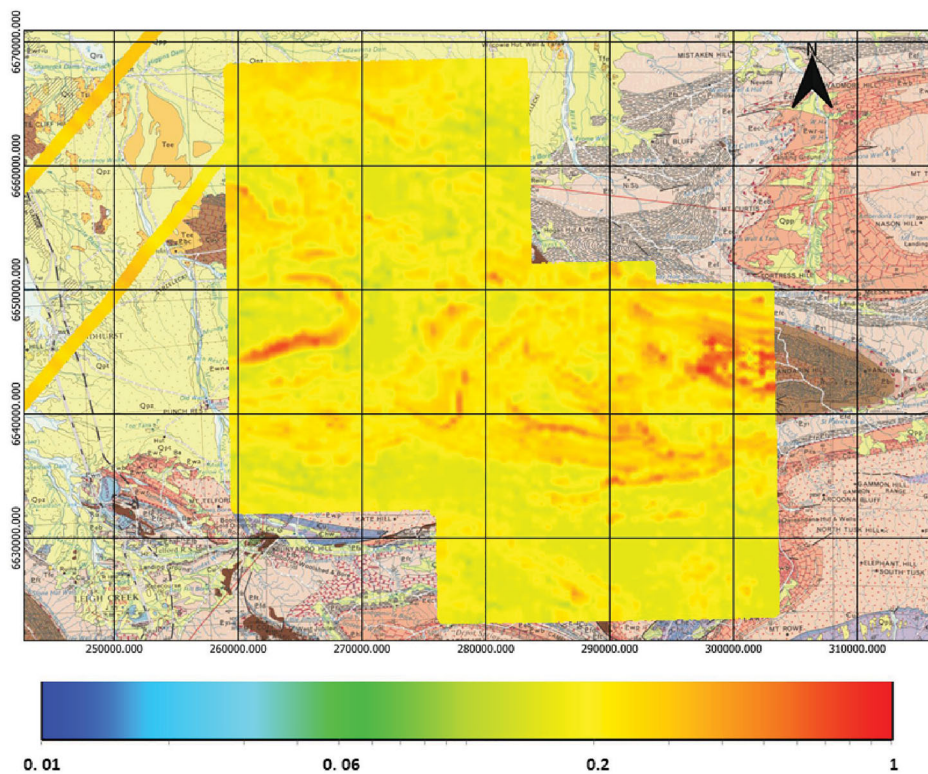


Figure 7. Sensitivity of IP scanner to the metric of decay rate interval C, illustrating some different zones of high sensitivity than for interval B in Figure 6.

effects (including negatives), we invert the data using the dispersive Cole–Cole model, in Pelton et al.’s notation (1978). The resulting inverted chargeability sections are compared graphically against the AIP scanner map values (e.g. Figure 10).

The good spatial correlation between the inverted chargeability and the scanner, as exemplified in Figure

10, confirms that the AIP scanner is indeed efficiently predicting the presence and location of measurable AIP effects (point 8 of the procedure above), and therefore also predicting where chargeability can be recovered (through layered earth inversion) from this specific AEM dataset. Had they been in poor agreement, we would have reiterated the procedure, changing some of the

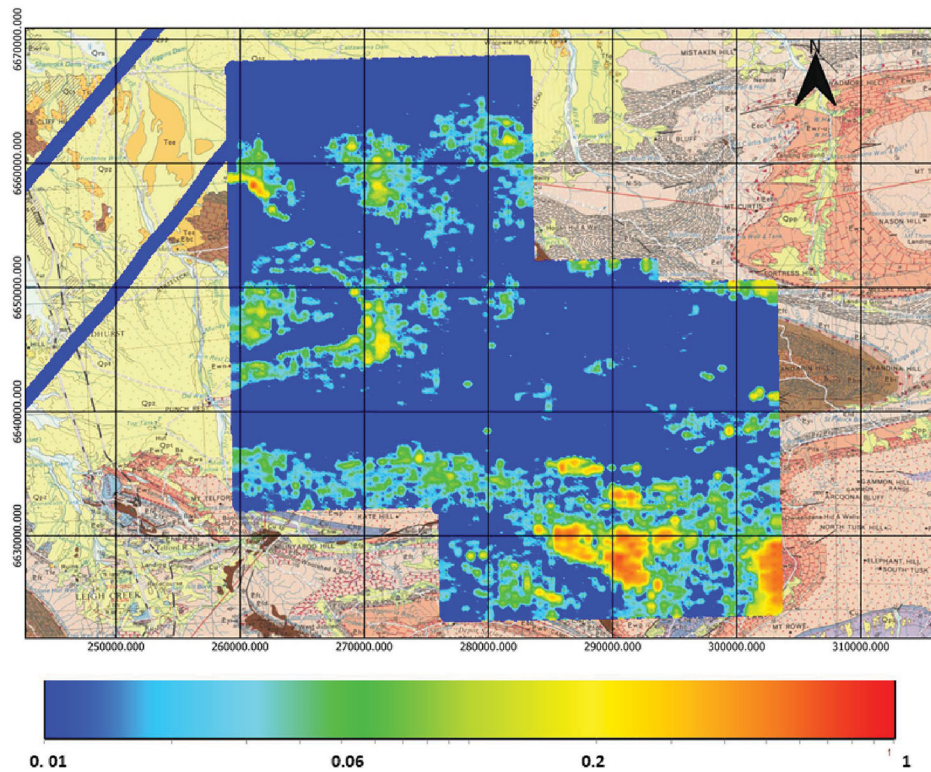


Figure 8. Sensitivity of IP scanner to the metric of the sum of negatives. This sensitivity map is spatially uncorrelated to the decay rate maps of Figures 6 and 7.

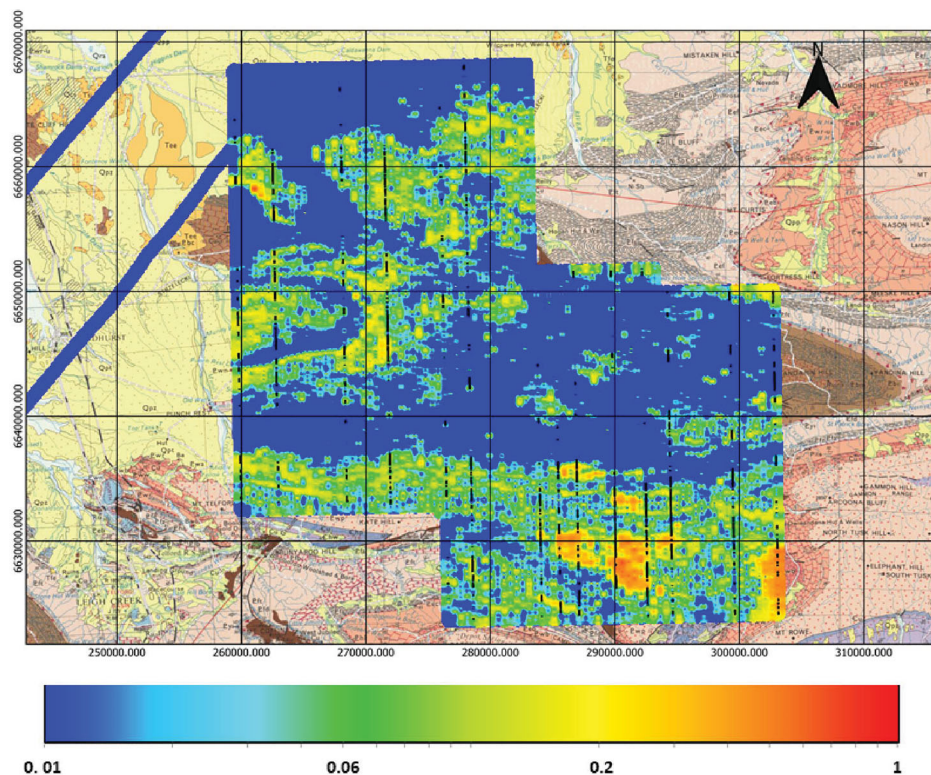


Figure 9. “AIP scanner” map, with dark blue = no AIP, yellow–orange–red = definite AIP, and light blue to green = possible AIP. The misfit from lines inverted without AIP modelling is superimposed as black dots for any misfit > 1, matching well with the scanner results.

parameters. While the AIP scanner indicates the degree of confidence with respect to the presence or not of IP effects in the AEM data, Figure 10 underscores that this does not reflect the magnitude or depth of the IP effect. The scanner prioritises areas for full AIP modelling, and

only the full modelling can extract chargeability, or correct resistivity. Conversely, a low probability of IP in the scanner results indicates areas where conventional resistivity inversions will be more reliable. The AIP scanning procedure is relatively fast and cheap compared to

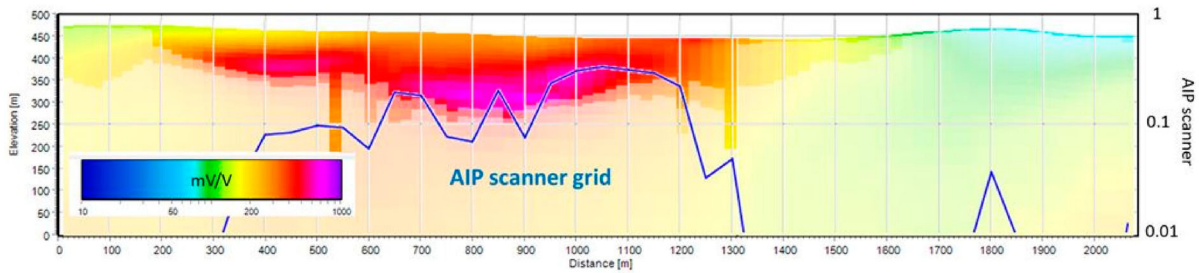


Figure 10. Inverted chargeability section compared against profile of AIP scanner values for one of the comparison lines. The depth of investigation is indicated via the faded portions of the section.

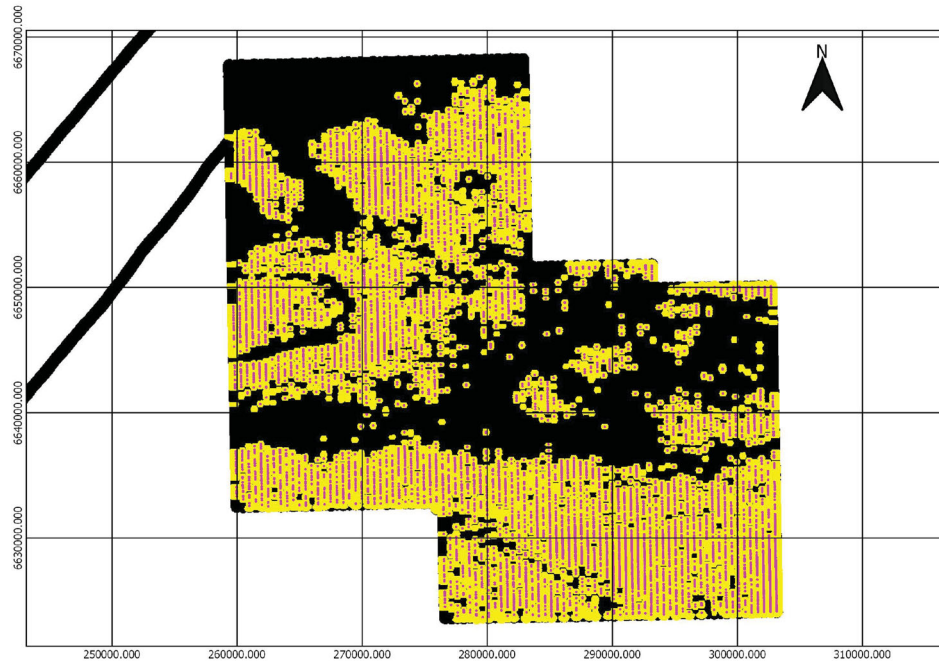


Figure 11. Spatial correlation between sum of negatives (pink) and IP scanner results (black = 0, yellow \neq 0 indicating probably AIP effects). Localised areas exist where AIP effects do not manifest as negative transients.

full AIP modelling over the entire area and is a useful precursor to guide the choice of more involved modelling. The methodology presented here is completely general, regardless of geology, signal levels, or AEM system, and has been applied to different datasets from around the world. The importance of negative transients to the final AIP scanner map varies. Figure 11 underscores that in the present case, the sum of negatives has a large but not ubiquitous influence on the resulting AIP scanner results – there are localised areas of AIP effects where no negative transients appear. These are the areas that would escape recognition via the conventional means of picking negative transients. In other circumstances, this relationship is not as strong (e.g. Dauti 2020).

Figure 12 compares the results obtained with and without AIP modelling, for the same line as in Figure 10. The first noteworthy point is the marked reduction in data misfit when AIP is modelled. Perhaps more interestingly from an exploration perspective, the choice to model with or without AIP effects would lead to different geological interpretations. In terms of the published geological map of the area, a conductor at depth in the

inversion with AIP can be assigned to the shales of the Tapley Hill Formation (Pft). This conductor is completely absent when inverting without AIP and so represents one of the most significant possible artefacts, where near-surface chargeability lowers the decay rate of transients sufficiently to mask the presence of a moderate conductor at depth. In terms of sediment-hosted base metal exploration, the inversion without AIP suggests a thin, well-defined conductor, potentially a shale unit, directly overlying a very resistive crystalline basement. As the first chemically reducing unit above the basement, such a shale is an attractive exploration target. When accounting for AIP, the near-surface conductor is more diffuse and no longer overlies anything more resistive than the general background of the section. This is a material change to the conceptual exploration target. The related IP section in Figure 10 suggests that the chargeability distribution responsible for these material changes is widespread and not associated with a discrete conductor (shale). This section represents some of the most dramatic changes due to the inclusion of IP effects, and yet the magnitude of the AIP scanner results does not predict this versus other areas with

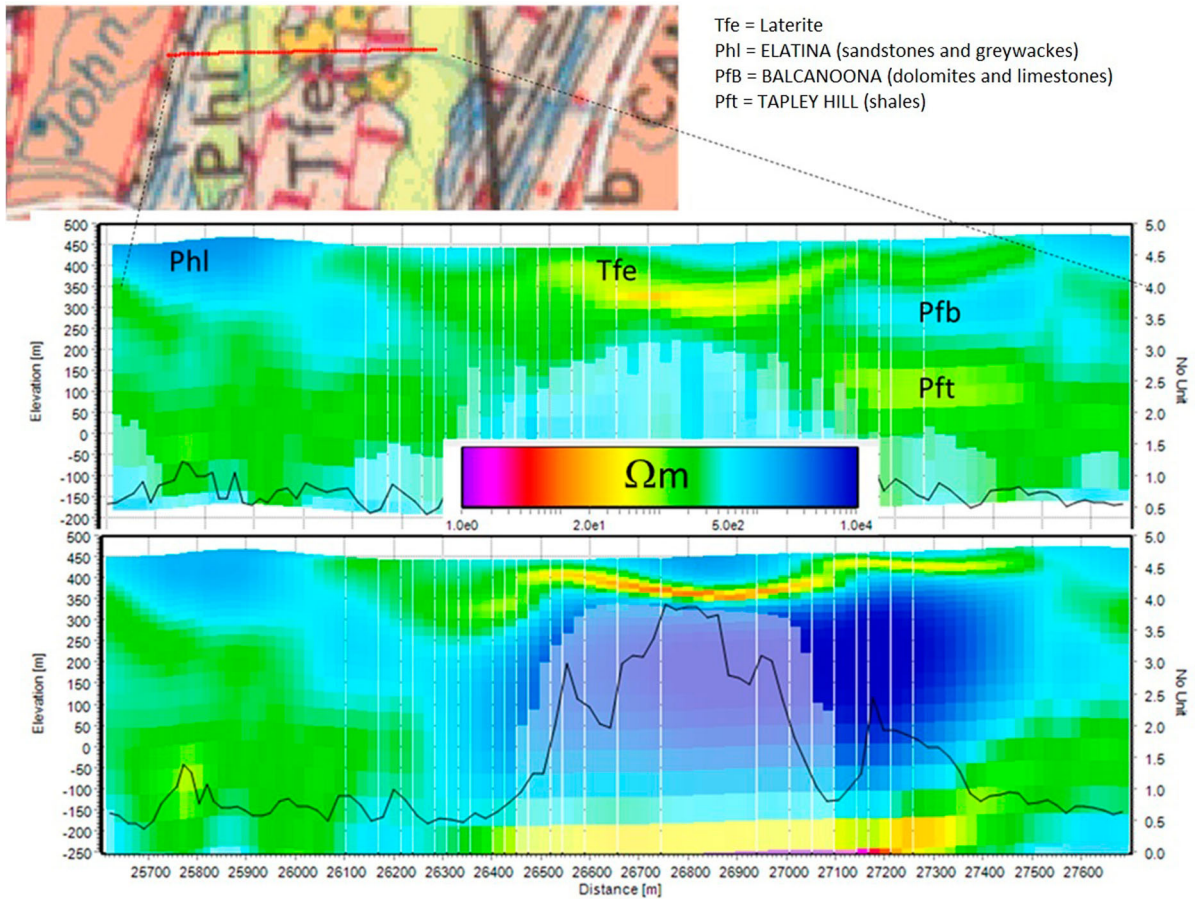


Figure 12. Resistivity models obtained with AIP modelling (top) and without AIP modelling (bottom) for the line identified in red on the geology map. Data misfit shown in black, to be read against the right axis. Depth of investigation is shown by the faded portions of the sections. Conductors and their geometries are sufficiently different to materially affect interpretation. Figure 7 contains the accompanying chargeability section.

larger scanner magnitudes, but less material effects on the resulting sections.

Figure 13 illustrates a situation with less material impact on the resistivity structure, but an intriguing chargeability result. Once again, an apparently thin and strong near-surface conductor, after accounting for IP effects, becomes more diffuse and has a greater depth extent. However, the interpretation of the dip and depth extent of the conductor as it continues to the right is unchanged between sections. Similarly, the moderately conductive left-hand side of the section is unchanged in gross character. The greatest change between sections is in the degree to which a conductivity contrast may indicate the location of a mapped fault as it continues under recent cover (drawn on the upper resistivity section of Figure 13). This contrast across the interpreted fault location is better defined over a larger depth interval when AIP is modelled. The corresponding chargeability section in Figure 14 places a discrete anomaly in the hanging wall of the interpreted fault. This becomes significant in terms of an exploration model of hydrothermal fluids travelling up or along a fault, carrying metals that react with a conductive (reducing) unit in the hanging wall, or depositing just below the unit if it

acted as a seal. Note that this relatively small, local anomaly could be rendered partly inaccurately by the 1D inversion (Lin et al. 2019). On the contrary, there is little doubt that the wider, less pronounced chargeable anomaly located to the right of the fault, which contains the discrete anomaly, is properly imaged by the 1D inversion.

Conclusions

The inclusion of IP effects when modelling AEM data can cause differences in resistivity distribution that are material to resource exploration, as well as provide a useful secondary dataset in terms of chargeability. It therefore behoves the end-users of AEM data to be aware of the degree and distribution of IP effects in the data. Our approach, valuable for historic and current datasets, has been to develop and test a novel tool called the “AIP scanner”. It combines analysis in the data space with limited model space analysis. Providing a robust indication of the location of AIP effects, the “AIP scanner” directly warns about portions of the resistivity models affected by artefacts if IP is (was) not modelled. This allows an end-user to make informed decisions about how to treat the affected data, as well

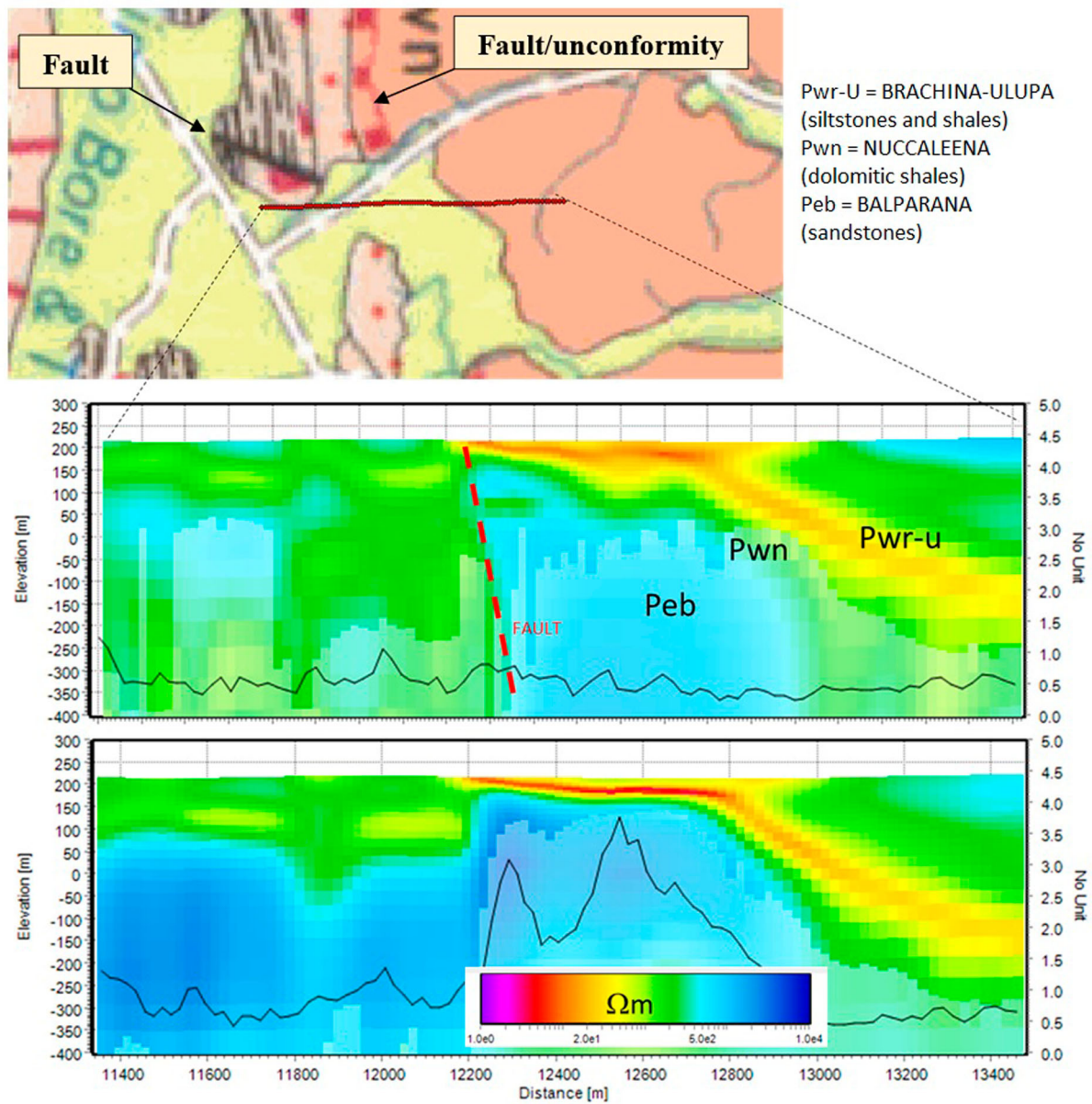


Figure 13. Resistivity models obtained with AIP modelling (top) and without AIP modelling (bottom) for the line identified on the geology map. The faulted unconformity is extended from the surface geology map, and there is another mapped fault intersecting this line at a high angle. Data misfit shown in black, to be read against the right axis. Depth of investigation is shown by the faded portions of the sections.

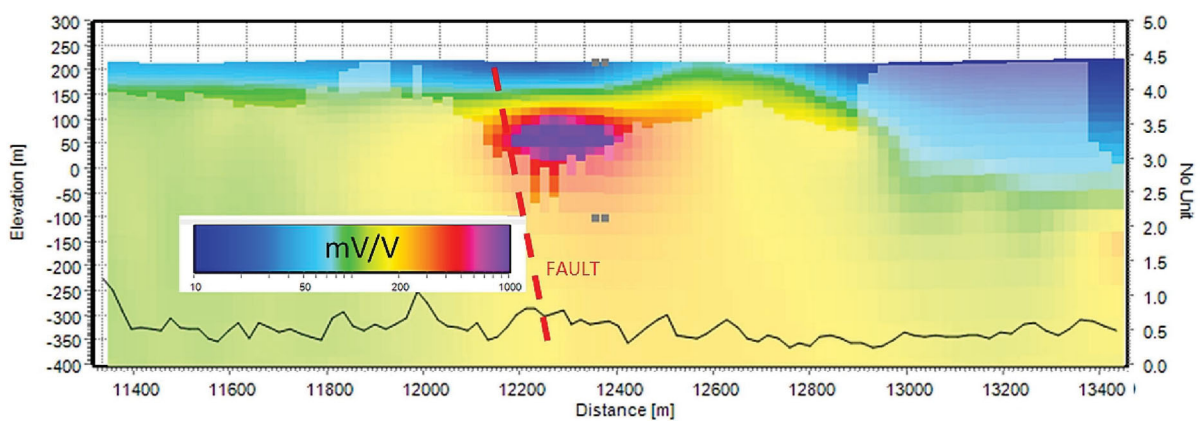


Figure 14. Chargeability section accompanying Figure 13. The fault is extended from the surface geology map in Figure 13. Data misfit shown in black, to be read against the right axis. Depth of investigation indicated via the faded portions of the section.

as where to trust conventionally inverted data without accounting for IP. Areas with a high probability of being affected by IP should be subject to more rigorous modelling of the AIP effects to correct the resistivity and extract the chargeability information. The “AIP scanner” can be applied quickly and cost efficiently to large datasets. It represents a valuable tool, for both explorers and government, that adds extra information to the AEM derived products and deliverables. Research is currently underway to explore the possibility of the AIP scanner providing some useful input to inversion parametrisation to reduce modelling efforts.

Acknowledgments

We thank First Quantum Minerals Ltd for providing the AEM dataset.

Disclosure statement

No potential conflict of interest was reported by the author(s).

Funding

This project has received funding from the European Union’s Horizon 2020 research and innovation programme [grant agreement number 776487].

References

- Buselli, G. 1982. The effect of near-surface superparamagnetic material on electromagnetic measurements. *Geophysics* 47: 1315–1324.
- Combrinck, M., and R. Wright. 2016. *Xcite: Great results require more than good data*. ASEG-PESA-AIG expanded abstract, Adelaide.
- Chen, T., G. Hodges, and A. Smiarowsky. 2015. *Extracting subtle IP from airborne time domain electromagnetic data*. SEG technical program extended abstracts 2015.
- Dauti, F. 2020. Robust scanning of AEM data for IP effects. Online conference, Near Surface Geoscience, EAGE.
- Kaminski, V., and A. Viezzoli. 2017. Modeling induced polarization effects in helicopter time-domain electromagnetic data: Field case studies. *Geophysics* 82: B49–B61.
- Kang, S., D. Fournier, and D. Oldenburg. 2017. Inversion of airborne geophysics over the DO-27/DO-18 kimberlites – Part 3: Induced polarization. *Interpretation* 5: T327–T340.
- Kwan, K., A. Prikhodko, J.M. Legault, G. Plastow, J. Xie, and K. Fisk. 2015. *Airborne inductive induced polarization chargeability mapping of VTEM data*. ASEG-PESA-AIG expanded abstract, Adelaide.
- Lin, C., G. Fiandaca, E. Auken, M.A. Couto, and A. Christiansen. 2019. A discussion of 2D induced polarization effects in airborne electromagnetic and inversion with a robust 1D laterally constrained inversion scheme. *Geophysics* 84 no. 2: E75–E88.
- Macnae, J. 2016. Quantitative estimation of intrinsic induced polarization and superparamagnetic parameters from airborne electromagnetic data. *Geophysics* 81 no. 6: E433–E446.
- McNeill, J.D. 1980. Applications of transient electromagnetic techniques. Technical Note TN-7 page 5, Geonics Limited, Mississauga, Ontario.
- Oldenburg, D.W., and S. Kang. 2015. *Recovering IP information in airborne-time domain electromagnetic data*. 24th ASEG-PESA meeting – Perth, Extended Abstract.
- Pelton, W.H., S.H. Ward, P.G. Hallof, W.R. Sill, and P.H. Nelson. 1978. Mineral discrimination and removal of inductive coupling with multifrequency IP. *Geophysics* 43: 588–609.
- Sattel, D., and P. Mutton. 2015. Modelling the superparamagnetic response of AEM data. *Exploration Geophysics* 46: 118–129.
- Smith, R., and G. West. 1988. *TEM coincident loop negatives and the loop effect*. *Exploration Geophysics* 19: 354–357.
- Viezzoli, A., V. Kaminski, and G. Fiandaca. 2017. Modeling induced polarization effects in helicopter time domain electromagnetic data: Synthetic case studies. *Geophysics* 82: E31–E50.
- Viezzoli, A., and G. Manca. 2020. On airborne IP effects in standard AEM systems: Tightening model space with data space. *Exploration Geophysics* 51 no. 1: 155–169.